

The link between extreme precipitation and convective organization in a warming climate: Global radiative convective equilibrium simulations

Angeline G. Pendergrass^{1,2}, Kevin A. Reed³, Brian Medeiros²

Corresponding author: Angeline G. Pendergrass, P.O. Box 3000, Boulder, CO 80307. (apgrass@ucar.edu)

¹CIRES, University of Colorado and
Climate and Global Dynamics Laboratory,
National Center for Atmospheric Research,
Boulder, Colorado, USA.

²Climate and Global Dynamics
Laboratory, National Center for
Atmospheric Research, Boulder, Colorado,
USA.

³School of Marine and Atmospheric
Sciences, State University of New York at
Stony Brook, Stony Brook, New York, USA.

Key Points.

- The rate of extreme precipitation change with warming can differ substantially from the rate of moistening.
- Convective organization varies with warming in climate model radiative-convective equilibrium simulations.
- The rate of extreme precipitation change with warming varies with changing convective organization.

The rate of increase of extreme precipitation in response to global warming varies dramatically across climate model simulations, particularly over the tropics, for reasons that have yet to be established. Here, we propose one potential mechanism: changing organization of convection with climate. We analyze a set of simulations with the Community Atmosphere Model version 5 (CAM5) with an idealized global radiative-convective equilibrium configuration forced by fixed SSTs varying in two-degree increments from 285 to 307 K. In these simulations, convective organization varies from semi-organized in cold sim-

ulations, disorganized in warm simulations, and abruptly becomes highly organized at just over 300 K. The change in extreme precipitation with warming also varies across these simulations, including a large increase at the transition from disorganized to organized convection. We develop an extreme-precipitation-focused metric for convective organization, and use this to explore their connection.

1. Introduction

The response of the hydrologic cycle to a changing climate is of utmost importance in evaluating mitigation and adaptation policies. Although some aspects of the hydrologic cycle have constraints imposed by the global energy budget, the factors driving others are not yet established. In particular, the balance between global-mean precipitation and radiative cooling is well understood, as is the expected increase in tropospheric specific humidity with surface warming; climate models robustly predict global-mean rainfall to increase at a lower rate than specific humidity [*Mitchell et al.*, 1987]. In contrast, there is a large spread in the extreme precipitation response, especially in the tropics [*O’Gorman and Schneider*, 2009a; *O’Gorman*, 2012]. If extreme precipitation events are driven by moisture convergence and circulation in extreme events changes little with warming, then extreme precipitation change will increase due to the “thermodynamic” effect of increasing saturation vapor pressure, and associated moist adiabatic lapse rate, with warming [e.g., *O’Gorman*, 2015]. Much of the change in the distribution of precipitation can be captured by shifting it to heavier rain rates and increasing the frequency of precipitation evenly at all rain rates [*Pendergrass and Hartmann*, 2014a]. These changes in the distribution of precipitation are connected to changes in warming, moistening, and the distribution of vertical velocity [*Pendergrass and Gerber*, 2016]. But the high rates of extreme precipitation increase in some climate models are not captured by movements of the distribution of precipitation; *Pendergrass and Hartmann* [2014a] call this deviation the “extreme mode.” If the circulation associated with extreme events were to dramatically change, the rate of change of extreme precipitation with warming would change as

well. Thus, changes in circulation could be one explanation for the large range in the rate of extreme precipitation change with warming in climate model simulations.

Extreme precipitation is often associated with organized convection, like tropical cyclones and mesoscale convective systems. Although organized convection has long been recognized as important, recent work has explored convection that can self-organize, both in observations and models. In numerical modeling studies of convection in idealized environments, convection forms randomly as the simulation begins, but aggregates into clusters as it evolves [Bretherton *et al.*, 2005; Muller and Held, 2012; Wing and Emanuel, 2014]. Depending on characteristics of the simulation (e.g., domain size, grid size, model formulation), the self-aggregated state represents a stable steady-state of the system, and eventually a single convective cluster forms and the rest of the model domain has a very dry, subsiding troposphere. Similar aggregation has recently been described in global climate models run in idealized configurations [Popke *et al.*, 2013; Reed *et al.*, 2015; Coppin and Bony, 2015]. Popke *et al.* [2013] showed that the mean climate of their idealized configuration closely resembles the tropical climate of comprehensive simulations with its parent model configuration. In these simulations, the degree of aggregation that occurs depends on the surface temperature [Held *et al.*, 2007; Wing and Emanuel, 2014; Bony *et al.*, 2016]. An important implication of this dependence is that the nature of organized convection may change with climate, altering the distribution of precipitation, including extreme precipitation [Tan *et al.*, 2015]. Two studies have examined changes in extreme precipitation in the context of organized convection [Muller, 2013; Singleton and

Toumi, 2013], but none have examined the effect of changing organization on extreme precipitation.

In this paper, we explore the relationship between extreme precipitation and convective aggregation in a set of climate model simulations with a range of surface temperatures. Using an idealized climate model configuration, we test the hypothesis that changes in organization influence extreme precipitation. Our intentions in this study are two-fold: (1) to illustrate a situation in which circulation, rather than moisture, drives a large increase in extreme precipitation, and (2) to develop metrics that quantify convective organization and relate it to extreme precipitation.

2. Model simulations

Twelve global radiative-convective equilibrium (RCE) simulations are run with CAM5, the atmospheric component of the Community Earth System Model (CESM). Each simulation has a uniform, fixed sea-surface temperature (SST) ranging from 285 to 307 K, runs for three years, and otherwise follows the methodology of *Reed et al.* [2015]. These simulations, along with global-RCE simulations from other climate models, have been used to explore the impact of surface temperature on convective anvil clouds [*Bony et al.*, 2016]; global RCE in CAM5 has also been used for convective process studies [*Reed and Chavas*, 2015; *Reed and Medeiros*, 2016]. The model uses the spectral element dynamical core on a cubed-sphere grid to solve the equations of motion [*Taylor and Fournier*, 2010; *Dennis et al.*, 2012]. Mean grid spacing is 111 km, which is typical for global climate simulations. The subgrid-scale physics are parameterized with schemes for moist turbulence, shallow convection, deep convection, cloud microphysics and macrophysics, radiative transfer, and

other processes; these are described in *Neale et al.* [2012]. The simplifications of the RCE configuration are: an aquaplanet with globally-uniform prescribed SST, spatially uniform and diurnally varying insolation with mean 340 W m^{-2} and equatorial solar zenith angle [following *Popke et al.*, 2013], and no planetary rotation (no Coriolis force). Greenhouse gas forcing is held fixed, with carbon dioxide at 348 ppm. Other aspects of the simulations follow *Reed et al.* [2015].

Figure 1 shows the mean precipitation from a randomly chosen month for each simulation. The number of precipitating regions and their spatial distribution changes across the simulations. Throughout this work, we will describe the simulations according to their prescribed SST and degree of organization: *cold* simulations are slightly organized, *warm* simulations are disorganized, and *hot* simulations are highly organized. As we will see in section 3.2, organization in the cold simulation is driven largely by long-lived precipitating events (Fig. 1 shows monthly rather than daily mean precipitation because the organization in the cold simulations is not visible in daily fields; the highly-organized systems in the hot simulations are nearly stationary, so they are evident in both daily and monthly precipitation). In the three cold simulations, there are multiple events which are dispersed, with patchy dry regions in between. The six warm simulations have more precipitating regions than the cold simulations, but each is smaller and weaker, with fewer dry regions. In each of the three hot simulations, precipitation is focused in one primary region (though there is more than one local maximum in two of the examples). The dry regions cover more of the remaining area in hot than in warm simulations.

Mean precipitation increases with warming in comprehensive climate model simulations [e.g., *Held and Soden* 2006], so we expect to see total rainfall increase with SST in our simulations. Figure 2a shows the globally-averaged precipitation calculated over each 3-year simulation, excluding the first six months for spinup. All simulations except 307 K reach a stable state in less than 6 months and maintain that state for the duration of the simulation, in contrast to results reported by *Coppin and Bony* [2015]. Mean precipitation increases from each simulation to the next, except from 289 to 291 K (the precipitation change from each simulation to the next relative to the prescribed 2-K SST change is shown in Fig. 2b). For reference, Fig. 2c shows the global-mean specific humidity from the lowest model level (referred to here as near-surface) in each simulation, with saturation specific humidity at the prescribed SST for reference.

Extreme precipitation is expected to increase more than mean precipitation with warming [e.g., *Trenberth*, 1999]. We quantify the extreme precipitation as the average precipitation rate from grid points with at least the 99th percentile of daily rainfall accumulation. This calculation entails, for each simulation, first forming the frequency distribution of daily accumulated precipitation following *Pendergrass and Hartmann* [2014b], excluding the first six months as spinup (as we did for mean precipitation). Then, we globally average this frequency distribution and determine its 99th percentile, including both wet and dry days [*Schär et al.*, 2016]. Finally, we find all grid-point-days with precipitation over the 99th percentile and area-average their precipitation rates. Figure 2d shows that extreme precipitation is largest in the three hot simulations, lowest in the warm simulations, and modestly large in the cold simulations.

Figure 2e shows the percentage change in extreme precipitation from each simulation to the next relative to the change in prescribed SST. Instead of increasing consistently by the same amount as the moisture holding capacity or average moisture, which would each be around $7\%K^{-1}$ in cold simulations and decrease slightly in warmer simulations, the extreme precipitation behaves quite differently. Between cold, semi-organized simulations ($<293\text{ K}$), extreme precipitation decreases with warming. Between warm, disorganized simulations ($297\text{-}301\text{ K}$), extreme precipitation increases by $5\text{-}7\%K^{-1}$. From the last warm, disorganized simulation (301 K) to the first hot, organized one (303 K), there is a dramatic increase of $73\%K^{-1}$. Between hot, organized simulations, extreme precipitation also increases, with erratic but smaller rates of increase. The magnitude of the change in extreme precipitation depends on the definition of extreme precipitation; when it is defined as the rain rate at a particular percentile (instead of all events above a percentile, as in Fig. 2e), the magnitude of its change with warming generally increases with increasing percentile. For example, the dramatic increase in extreme precipitation from 301 to 303 K has a magnitude of $20\%K^{-1}$ at the 99th percentile and $149\%K^{-1}$ at the 99.9th percentile.

3. Convective Organization

In order to study how convective organization relates to extreme precipitation, we must quantify it. Some metrics that have been used in the past to quantify convective organization include the dry area fraction [e.g., *Coppin and Bony, 2015*], and the number, size, and distance between contiguous regions of brightness temperature below a threshold [*Mapes and Houze, 1993; Tobin et al., 2012*]. Dry fraction is not as useful a metric in realistic domains which we aspire to examine, and OLR-based metrics are problematic when exam-

ining global warming simulations because we expect mean OLR to change with warming. To overcome these challenges and facilitate comparison with precipitation, we develop a precipitation-based metric for convective organization. Our metric is focused on events, rather than whole domains, and builds on *Tobin et al.* [2012]. Instead of an OLR-based threshold, we use a precipitation intensity threshold: grid cells with precipitation rates of at least the 99th percentile.

3.1. Event identification and tracking

Our precipitation-centric event identification and tracking algorithm works as follows. First, we calculate the 99th percentile of precipitation as described in Section 2. Then, we identify regions of contiguous grid cells with >99th-percentile precipitation for each day of the simulation. Next, we track the contiguous regions from one day to the next. Regions are considered to be contiguous if there is an overlap of at least 25% of the area of the smaller of the regions. Most previous work uses 50% overlap and 6-hourly data. We use daily data because that is the frequency at which some fields were saved; we chose the 50% overlap threshold through testing on organized simulations. We accommodate merging and splitting by requiring that each event constitutes only one contiguous region per day; in cases of conflict the event with the largest overlapping area continues, and in a tie, the longer-lived event is chosen. Tracking is done on the native cubed-sphere grid, which has the advantage that all grid cells have similar area and also allows uninterrupted movement of events across the poles.

3.2. Convective Aggregation Index

Using the event identification and tracking algorithm, we quantify convective organization in each simulation. We define a Convective Aggregation Index (CAI),

$$CAI \equiv \frac{ND}{T}, \quad (1)$$

where N is the average number of events, D is the average distance between events (arithmetic mean cluster distance D_1 , as defined in *Tobin et al.* [2012]), and T is the average event duration, weighted by event area. Smaller CAI implies more organization. CAI extends the metric developed in *Tobin et al.* [2012] by incorporating event duration, which is necessary to capture the organization in the cold simulations. The high degree of organization in the hot simulations is robust to different metrics.

Figure 2f-i show N , D , T , and the CAI for each simulation. Convective organization is a minimum at moderate, tropical-like temperatures (Fig. 2i). CAI captures the essential organizing behavior apparent in Fig. 1: cold simulations that are moderately organized, decreasing organization through the warm simulations, and an abrupt transition to high organization in the three hottest simulations. N is largest in the cold simulations, decreases abruptly from 293 to 295 K, and decreases again from 301 to 303 K. D quantifies the spacing between events: organization increases when events clustered in space, leaving a larger dry region. When events are clustered, the convection is more organized and D is small. D is relatively steady until 303 K, when it decreases abruptly. T is longest in 303 and 305 K simulations, moderate in the cold and the hottest simulations, and shortest in the warm simulations.

An alternative quantification of organization is the fraction of total rain falling in extreme events (>99th-percentile precipitation) as a function of the event size (Fig. 2k). Extreme-event precipitation is binned by the logarithm of event area into 100 bins with exponentially increasing width, with edges distributed evenly in logarithmic space from $\log 10^4$ to $\log 10^7$ m², and then normalized by the simulation's total precipitation. Each resulting distribution of precipitation fraction by event area sums to the fraction of total precipitation falling in all extreme events (Fig. 2j). The fraction of precipitation falling in extreme events is higher for more organized simulations. In cold and warm simulations, the distribution of precipitation by extreme event size is centered at around 2×10^5 km². In the hot simulations, the distribution is bimodal: some precipitation falls in events with the same size as cooler simulations, but more falls in larger events ($\sim 3 \times 10^6$ km²). The hottest simulation is an exception, with the most precipitation from events of moderate size. Despite that cold and warm simulations have peak precipitation fraction at similar event size, a larger fraction of rain falls in extreme events in the cold simulations compared to the warm ones because event duration is longer in the cold simulations (Fig. 2h).

The contributions of large-scale and convective precipitation to the rain amount distribution provide another indication that the cold and hot simulations are more organized than the warm ones (Fig. S1, following *Pendergrass and Hartmann 2014a*). In the hot simulations, the rain amount distribution has an extension to very heavy rain rates which includes a substantial contribution from from large-scale precipitation, indicating that the circulations involved are resolved. The cold simulations also have substantial contributions from large-scale precipitation centered heavy rain rates relative to their distributions. In

contrast, in the warm simulations, the most large-scale precipitation occurs at rain rates that also have substantial convective precipitation.

4. Circulation changes with convective organization

Figure 3 shows 850 hPa vertical velocity, near-surface specific humidity, and profiles of temperature and vertical velocity area-averaged over events with >99th-percentile precipitation for each simulation. The 850 hPa vertical velocity is strongest in the coldest and hottest simulations, and weakest for the warm simulations. The weakening from cold to warm simulations is gradual, while the strengthening from warm to hot simulations is abrupt between 301 and 303 K. The specific humidity, on the other hand, increases steadily with warming. Temperature increases throughout the troposphere with increasing SST, with additional amplified of warming aloft in the hot simulations.

The vertical velocity profile averaged over all extreme events in each simulation is shown in Fig. 3d. The maximum vertical velocity achieved occurs between 500 and 600 hPa in the cold simulations. These simulations have extreme events with convection reaching the tropopause (which rises with SST). The warm simulations have the weakest vertical velocities throughout the column, with some showing a local minimum around 700 hPa, indicating that extreme events are shallow. The hot simulations have vertical velocity maxima near 800 hPa, shallower than the cold simulations, but with strong ascent over a larger fraction of the troposphere.

5. Mechanisms of extreme precipitation change

To isolate the dynamic effects of changing vertical velocity from the thermodynamic effects of changing temperature, we apply the extreme precipitation scaling from *O’Gorman*

and Schneider [2009a] to the CAM5 global-RCE simulations, and make a set of sensitivity calculations (Fig. 4). The extreme precipitation scaling is the integral of condensed water due to vertical advection of moisture along a moist adiabat,

$$P_e \approx \int_{p_t}^{p_s} \frac{dp}{g} \omega \frac{dq_s}{dp} \Big|_{\theta^*, T_e}, \quad (2)$$

where P_e is the >99th-percentile precipitation, p_t is the tropopause pressure (the highest level with a lapse rate of 2 K km⁻¹), p_s is the surface pressure, g is the gravitational constant, ω is the vertical velocity profile, and dq_s/dp is the vertical derivative of saturation vapor pressure. The extremes scaling is calculated on profiles of temperature T_e (Fig. 3c) and vertical velocity (Fig. 3d) area-averaged over all >99th-percentile events in each simulation, otherwise following *O’Gorman and Schneider* [2009a]. We did not use grid-point or event-averaged profiles because our tests indicate that these result in less accurate fits to the change in extreme precipitation across the simulations. We speculate that the difference arises because the scaling does not account for local downdrafts associated with horizontal advection, which averaging removes.

In addition to applying the extremes scaling to the profiles from each simulation (Fig. 4a), we perform three sensitivity calculations which isolate the effects of varying the anomalous temperature profile, vertical velocity, and temperature. We define the anomalous temperature profile as the temperature at each level in the troposphere minus SST. To isolate the effect of the anomalous temperature profile, we fix the vertical velocity profile at its value in the 299 K simulation, set the surface temperature to 299 K, and allow the anomalous temperature profile to vary. Results are not sensitive to the choice of 299 K as the base simulation. To isolate the effect of vertical velocity, we allow it to

vary while holding SST and temperature profile fixed at values from the 299 K simulation (Fig. 4c). To isolate the effect of temperature, we allow only SST to vary, while holding vertical velocity and anomalous temperature profiles fixed at values from the 299 K simulation (Fig. 4d).

The extremes scaling accurately captures the change in extreme precipitation in most cases (Fig. 4a; c.f. Fig. 2e). It captures the decrease in extreme precipitation with warming in the cold simulations, the modest increase with warming in the warm simulations, the jump to much higher extreme precipitation rates from the 301 to 303 K simulations, and the return to more modest but erratic changes between hot simulations.

Varying only anomalous temperature profile recovers some aspects of the extreme precipitation change, but not others (Fig. 4b). Among the cold simulations, the extreme precipitation change is muted, decreasing in one case. There is a local maximum at the transition from cold to warm, and another at the transition from warm to hot. But the transition from warm to hot has an increase of $6.7\% \text{ K}^{-1}$, far less than the $73\% \text{ K}^{-1}$ in the simulations.

Varying vertical velocity captures important features of the extreme precipitation change, particularly the large increase from warm to hot simulations ($60\% \text{ K}^{-1}$). Furthermore, because we calculate the change in extreme precipitation from one simulation to the next, the increases are cumulative (e.g. Fig. 2e). Thus, the variation in vertical velocity alone recovers the transition of extreme precipitation magnitude to much larger values, which is sustained across the hot simulations. The extreme precipitation decrease between cold simulations and the variation between hot simulations are also captured, though the

increase in extreme precipitation between warm simulations is underestimated in this sensitivity calculation.

The effect of increasing surface temperature (Fig. 4d) is to increase extreme precipitation by $6.6\% \text{ K}^{-1}$ from one simulation to the next at cold temperatures, with steadily less increase as SST increases until the $4.0\% \text{ K}^{-1}$ between the two hottest simulations. The effect of increasing temperature is important, but it is not responsible for the rich behavior of extreme precipitation change with warming that we see in our simulations.

The sum of the three sensitivity calculations closely recovers the scaling of all three variations together (i.e. Figs. 4b-d sum to Fig. 4a). These sensitivity calculations show that while extreme precipitation change varies due to changing circulation as well as temperature, the large increase at the transition from disorganized to organized states only occurs in response to changing circulation. Within any regime, the variation in extreme precipitation scaling is small, but between regimes the difference can be large.

6. Discussion and Conclusion

We have examined a set of idealized CAM5 simulations in the global-RCE configuration forced by fixed SSTs varying from 285 to 307 K. In this set of simulations, convective organization varies from moderate in the coldest simulations, to disorganized in warm simulations, to highly organized in hot simulations. We have shown that while moisture and global-mean precipitation increase with warming across most of the simulations, extreme precipitation does not steadily increase with warming; instead, it varies dramatically. Quantifying extreme precipitation by events with at least 99th-percentile daily precipitation, it can increase by over $70\% \text{ K}^{-1}$ or decrease by more than $10\% \text{ K}^{-1}$. Using

a scaling for extreme precipitation based on condensation due to vertical advection along moist adiabats, we show that the variation in extreme precipitation change across the simulations can be explained largely by the variation in circulation, with temperature change playing an important but secondary role.

Due to the nature of the experimental setup, some important cautions regarding our results deserve to be stated explicitly. First, we do not expect the temperature thresholds here to generalize to Earth or even other models, because the temperatures at which convective organization changes states are known to vary in different models according to factors including but not limited to resolution, dynamical core, and parameterization schemes. Furthermore, our configuration does not include land, the effects of rotation, or the spatial pattern of insolation. For these reasons, it is important to evaluate the relevant relationships and their mechanisms in more comprehensive climate model simulations, convection-permitting simulations, and observations; we cannot assume that these same behaviors are relevant for Earth on the basis of this analysis. That said, *Popke et al.* [2013] indicate that global-RCE simulations could be relevant for understanding comprehensive climate models. We would expect our results to be most relevant to the equatorial region, where tropical cyclones and baroclinic eddies play a minor role driving atmospheric circulation.

Nonetheless, in this study, our goals were to illustrate a situation in which changes in extreme precipitation with warming vary dramatically due to changes in circulation, and to develop metrics quantifying convective organization and its relationship to extreme precipitation. We have presented one potential mechanism for the large increases in

extreme precipitation with warming in some climate models (the “extreme mode” from *Pendergrass and Hartmann 2014a*): changing convective organization. It remains to be seen whether this mechanism plays a role in comprehensive climate model simulations or observations, but the tools and understanding developed here enable these investigations. This study demonstrates that one answer to the WCRP grand challenge question *What role does convective aggregation play in climate?* [*Bony et al., 2015*] is that it might be important for understanding changes in extremes.

Acknowledgments. We thank two anonymous reviewers for their insightful suggestions which improved the manuscript and Robert Wills for helpful discussion. The CAM5 output presented in this study is available on NCAR’s Yellowstone computing platform. Matlab code to calculate rainfall distributions and identify and track regions can be found at github.com/apendergrass. Derived data shown in Figs. 2-4 is included in the Supplementary Information. AGP was supported by the CIRES Visiting Fellowship at the University of Colorado and the ASP Postdoctoral Research Fellowship at NCAR. BM and AGP were supported by the Regional and Global Climate Modeling Program of the U.S. Department of Energy’s Office of Science, Cooperative Agreement DE-FC02-97ER62402. NCAR is sponsored by the National Science Foundation. We acknowledge high-performance computing support from Yellowstone ([ark:/85065/d7wd3xhc](https://doi.org/10.7554/ark:/85065/d7wd3xhc)) provided by NCAR’s Computational and Information Systems Laboratory, also sponsored by the National Science Foundation.

References

- Bony, S., B. Stevens, D. M. Frierson, C. Jakob, M. Kageyama, R. Pincus, T. G. Shepherd, S. C. Sherwood, A. P. Siebesma, A. H. Sobel, and M. Watanabe (2015). Clouds, circulation and climate sensitivity. *Nat. Geosci.*, *8*(4), 261–268, doi:10.1038/NGEO2398.
- Bony, S., B. Stevens, D. Coppin, T. Becker, K. A. Reed, A. Voigt, and B. Medeiros (2016), Thermodynamic control of anvil-cloud amount, *Proc. Natl. Acad. Sci.*, *119*(32), 8927–8932, doi:10.1073/pnas.1601472113.
- Bretherton, C. S., P. N. Blossey, and M. Khairoutdinov (2005), An Energy-Balance Analysis of Deep Convective Self-Aggregation above Uniform SST., *J. Atmos. Sci.*, *62*, 4273–4292, doi:10.1175/JAS3614.1.
- Coppin, D., and S. Bony (2015), Physical mechanisms controlling the initiation of convective self-aggregation in a general circulation model, *J. Adv. Model. Earth Syst.*, *7*(4), 2060–2078, doi:10.1002/2015MS000571.
- Dennis, J., J. Edwards, K. J. Evans, O. N. Guba, P. H. Lauritzen, A. A. Mirin, A. St-Cyr, M. A. Taylor, and P. H. Worley (2012), CAM-SE: A scalable spectral element dynamical core for the Community Atmosphere Model, *Int. J. High Perf. Comput. Appl.*, *26*, 74–89, doi:10.1177/1094342011428142.
- Held, I. M., and B. J. Soden (2006), Robust responses of the hydrological cycle to global warming, *J. Clim.*, *19*(21), 5686–5699, doi:10.1175/JCLI3990.1.
- Held, I. M., M. Zhao, and B. Wyman (2007), Dynamic Radiative Convective Equilibria Using GCM Column Physics, *J. Atmos. Sci.*, *64*, 228, doi:10.1175/JAS3825.11.

- Mapes, B. E., and R. A. Houze (1993), Cloud clusters and superclusters over the oceanic warm pool, *Mon. Weather Rev.*, *121*(5), 1398–1416.
- Mitchell, J. F., Wilson, C. A., and Cunnington, W. M. (1987). On CO₂ climate sensitivity and model dependence of results. *Q. J. R. Meteorol. Soc.*, *113*(475), 293–322, doi:10.1002/qj.49711347517.
- Muller, C. (2013), Impact of convective organization on the response of tropical precipitation extremes to warming, *J. Clim.*, *26*(14), 5028–5043, doi:10.1175/JCLI-D-12-00655.1.
- Muller, C. J., and I. M. Held (2012), Detailed Investigation of the Self-Aggregation of Convection in Cloud-Resolving Simulations, *J. Atmos. Sci.*, *69*, 2551–2565, doi:10.1175/JAS-D-11-0257.1.
- Neale, R. B., C. C. Chen, A. Gettelman, P. H. Lauritzen, S. Park, D. L. Williamson, A. J. Conley, R. Garcia, D. Kinnison, J. F. Lamarque, D. Marsh, M. Mills, A. K. Smith, S. Tilmes, F. Vitt, P. Cameron-Smith, W. D. Collins, M. J. Iacono, R. C. Easter, S. J. Ghan, X. Liu, P. J. Rasch, and M. A. Taylor (2012), Description of the NCAR Community Atmosphere Model (CAM 5.0), *NCAR Tech. Note NCAR/TN-486+STR*, National Center for Atmospheric Research, Boulder, Colorado, 282 pp.
- O’Gorman, P. A. (2012), Sensitivity of tropical precipitation extremes to climate change, *Nat. Geosci.*, *5*(10), 697–700, doi:10.1038/NGEO1568.
- O’Gorman, P. A., and T. Schneider (2009a), The physical basis for increases in precipitation extremes in simulations of 21st-century climate change, *Proc. Natl. Acad. Sci.*, *106*(35), 14,773–14,777, doi:10.1073/pnas.0907610106.

- O’Gorman, P. A. (2015), Precipitation extremes under climate change, *Current Climate Change Reports*, 1(2), 49–59, doi:10.1007/s40641-015-0009-3.
- Pendergrass, A. G., and D. L. Hartmann (2014a), Changes in the distribution of rain frequency and intensity in response to global warming, *J. Clim.*, 27(22), 8372–8383, doi:10.1175/JCLI-D-14-00183.1.
- Pendergrass, A. G., and D. L. Hartmann (2014b), Two modes of change of the distribution of rain, *J. Clim.*, 27(22), 8357–8371, doi:10.1175/JCLI-D-14-00182.1.
- Pendergrass, A. G., and E. P. Gerber (2016), The rain is askew: Two idealized models relating vertical velocity and precipitation distributions in a warming world, *J. Clim.*, doi:10.1175/JCLI-D-16-0097.1.
- Popke, D., B. Stevens, and A. Voigt (2013), Climate and climate change in a radiative-convective equilibrium version of ECHAM6, *J. Adv. Model. Earth Syst.*, 5, 1–14, doi:10.1029/2012MS000191.
- Reed, K. A., and D. R. Chavas (2015), Uniformly rotating global radiative-convective equilibrium in the community atmosphere model, version 5, *J. Adv. Model. Earth Syst.*, 7(4), 1938–1955, doi:10.1002/2015MS000519.
- Reed, K. A., and B. Medeiros (2016), A reduced complexity framework to bridge the gap between agcms and cloud-resolving models, *Geophys. Res. Lett.*, 43(2), 860–866, doi:10.1002/2015GL066713, 2015GL066713.
- Reed, K. A., B. Medeiros, J. T. Bacmeister, and P. H. Lauritzen (2015), Global radiative-convective equilibrium in the Community Atmosphere Model, Version 5, *J. Atmos. Sci.*, 72(5), 2183–2197, doi:10.1175/JAS-D-14-0268.1.

- Schär, C., N. Ban, E. M. Fischer, J. Rajczak, J. Schmidli, C. Frei, F. Giorgi, T. R. Karl, E. J. Kendon, A. M. K. Tank, et al. (2016), Percentile indices for assessing changes in heavy precipitation events, *Clim. Change*, pp. 1–16, doi:10.1007/s10584-016-1669-2.
- Singleton, A., and R. Toumi (2013), Super-Clausius–Clapeyron scaling of rainfall in a model squall line, *Q. J. R. Meteorol. Soc.*, *139*(671), 334–339, doi:10.1002/qj.1919.
- Tan, J., C. Jakob, W. B. Rossow, and G. Tselioudis (2015), Increases in tropical rainfall driven by changes in frequency of organized deep convection, *Nature*, *519*(7544), 451–454, doi:10.1038/nature14339.
- Taylor, M. A., and A. Fournier (2010), A compatible and conservative spectral element method on unstructured grids, *J. Comput. Phys.*, *229*, 5879–5895, doi:10.1016/j.jcp.2010.04.008.
- Tobin, I., S. Bony, and R. Roca (2012), Observational evidence for relationships between the degree of aggregation of deep convection, water vapor, surface fluxes, and radiation, *J. Clim.*, *25*(20), 6885–6904, doi:10.1175/JCLI-D-11-00258.1.
- Trenberth, K. E. (1999), Conceptual framework for changes of extremes of the hydrological cycle with climate change, *Wea. Clim. Extremes*, pp. 327–339, doi:10.1007/978-94-015-9265-9_18.
- Wing, A. A., and K. A. Emanuel (2014), Physical mechanisms controlling self-aggregation of convection in idealized numerical modeling simulations, *J. Adv. Model. Earth Syst.*, *6*(1), 59–74, doi:10.1002/2013MS000269.

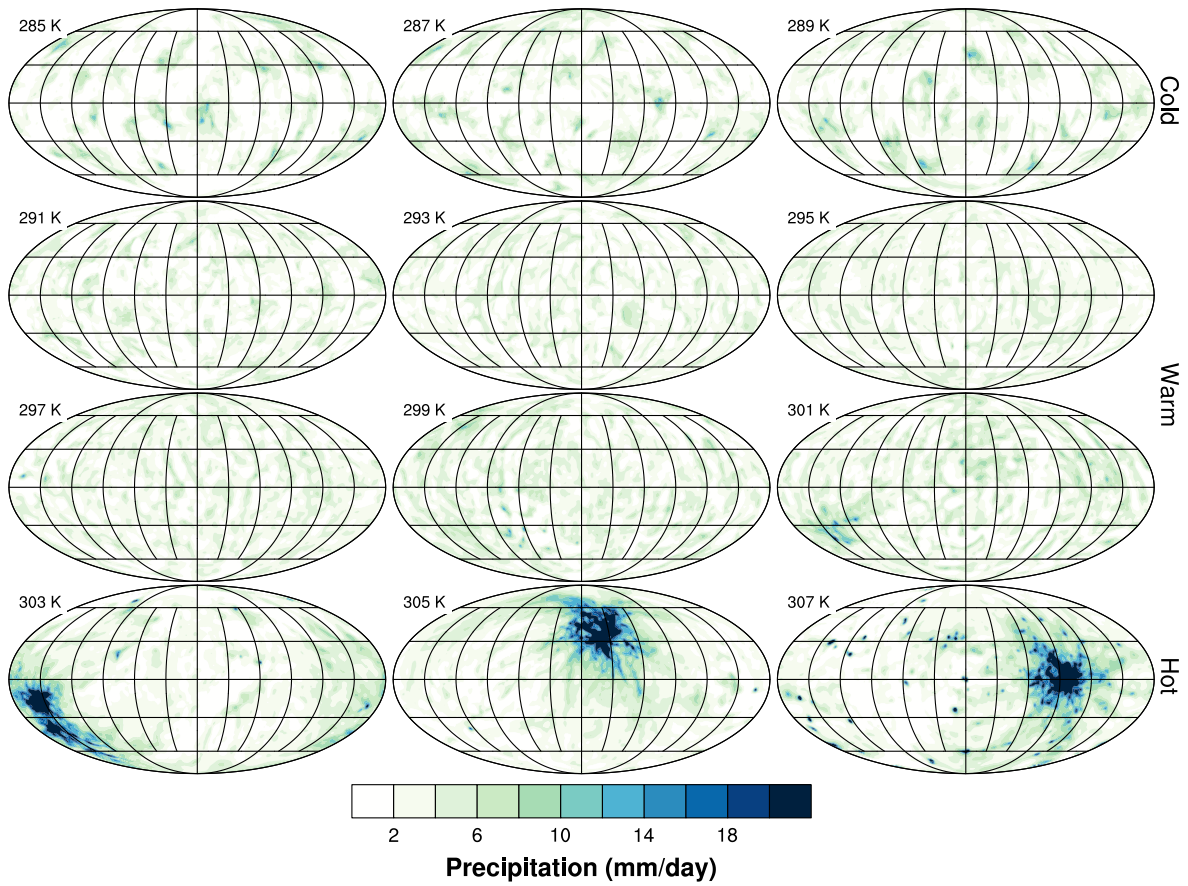


Figure 1. Monthly mean precipitation from a randomly chosen month for each simulation, with specified SST at top-left.

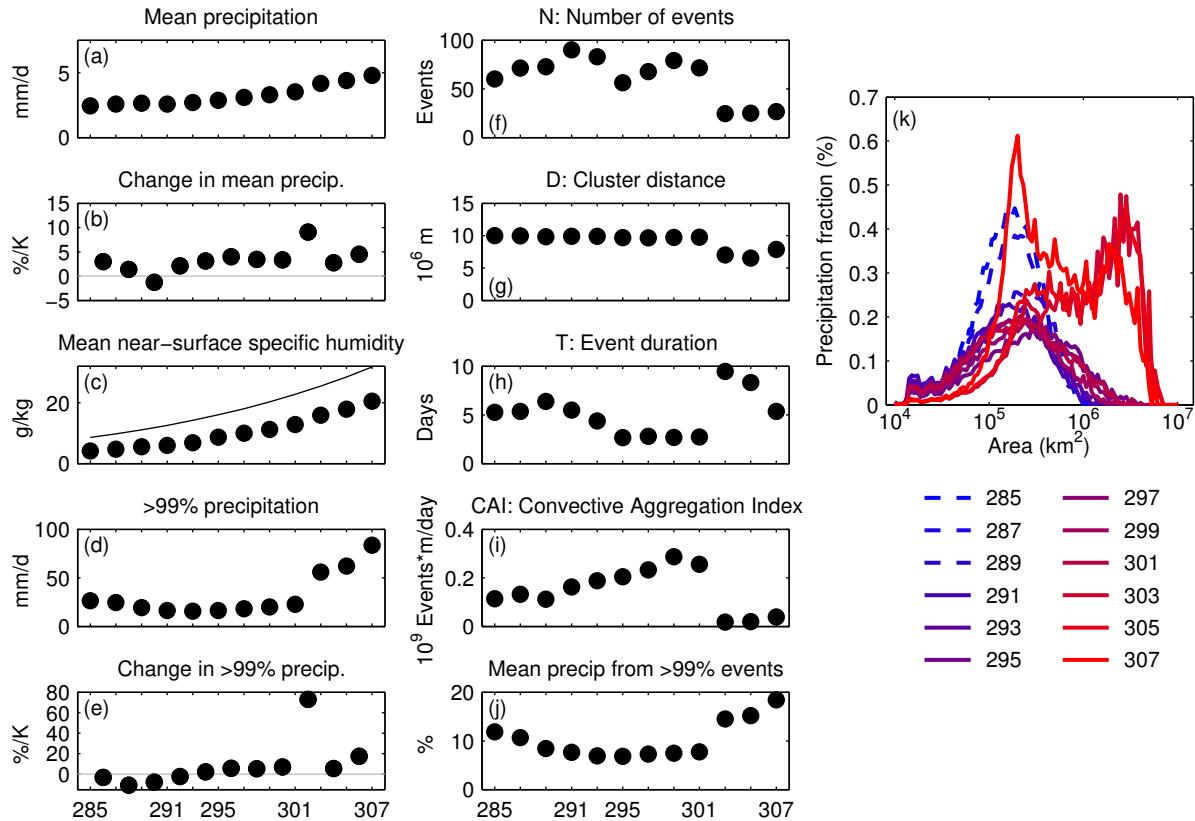


Figure 2. (a) Global-mean precipitation, (b) change in mean precipitation, (c) global-mean near-surface specific humidity and saturation specific humidity at each simulation’s specified SST (line), (d) extreme precipitation (the average rain rate of events over the 99th percentile), and (e) the change in extreme precipitation between simulations with 2-K SST increments in global RCE CAM5 simulations. (f) Number of regions N , (g) distance between events (cluster distance D), (h) event duration T , and (i) Convective Aggregation Index (Eq. 1). (j) Fraction of total precipitation from events with >99th-percentile rain rate. (k) Fraction of rain contributed by events as a function of event area (see text for description).

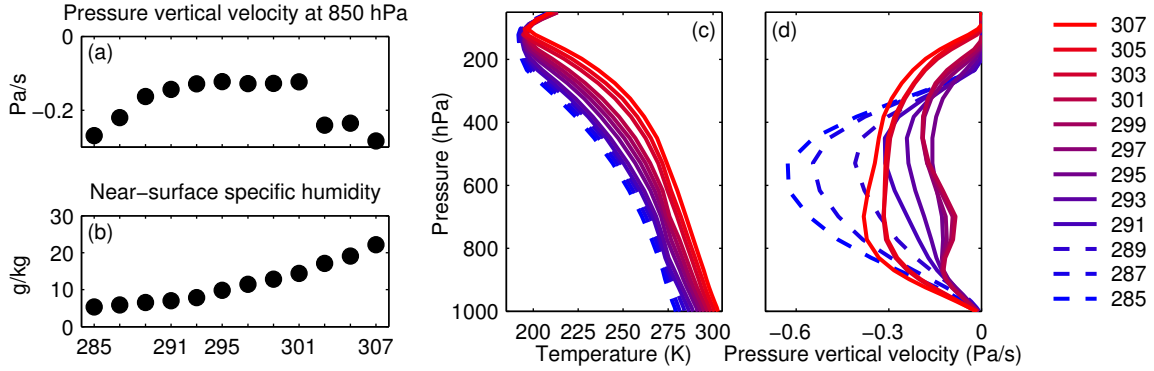


Figure 3. (a) Pressure vertical velocity at 850 hPa, (b) near-surface specific humidity (from the lowest model level), (c) temperature and (d) vertical velocity profiles averaged over all events with >99th-percentile daily precipitation.

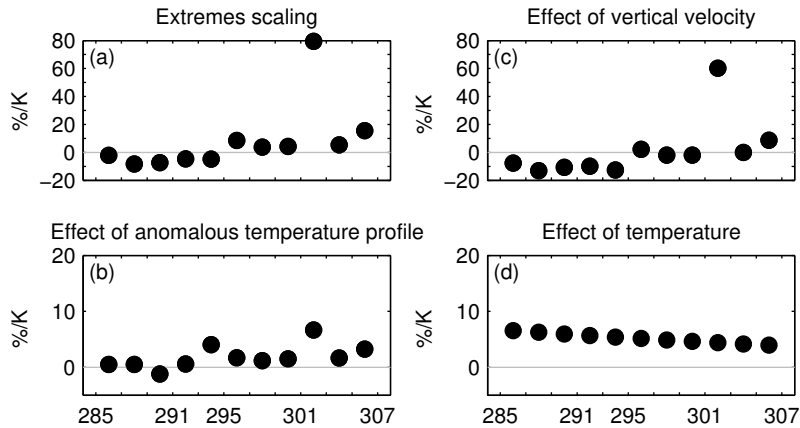


Figure 4. (a) Extreme precipitation scaling based on area-averaged profiles of ω and temperature from events with >99th-percentile precipitation. (b) Extremes scaling varying only the anomalous temperature profile. (c) Extremes scaling varying only the vertical velocity profile. (d) Extremes scaling varying only the SST. See text for details.

Supporting Information for “The link between extreme precipitation and convective organization in a warming climate: Global radiative-convective equilibrium simulations”

Angeline G. Pendergrass^{1,2}, Kevin A. Reed³, Brian Medeiros²

Contents of this file

¹CIRES, University of Colorado and
Climate and Global Dynamics Laboratory,
National Center for Atmospheric Research,
Boulder, Colorado, USA.

²Climate and Global Dynamics
Laboratory, National Center for
Atmospheric Research, Boulder, Colorado,
USA.

³School of Marine and Atmospheric
Sciences, State University of New York at
Stony Brook, Stony Brook, New York, USA.

1. Figure S1
2. Tables S1 to S4

Additional Supporting Information

1. Captions for Datasets S1 to S3

Introduction This supporting information provides an addition supporting figure, and includes the numerical values from Figs. 2-4 of the main text. Tables S1 and S2 show the data from Fig. 2a-j, Table S3 shows the data from Fig. 3a,b, and Table S4 shows the data from Fig. 4. Numerical values from Fig. 2k and Figs. 3c,d are included as additional Data Sets.

Data Set S1. The fraction of total precipitation as a function of event area (values shown in Fig. 2k).

Data Set S2. Temperature profile in each simulation (values from Fig. 3c).

Data Set S3. Vertical velocity profile in each simulation (values from Fig. 3d).

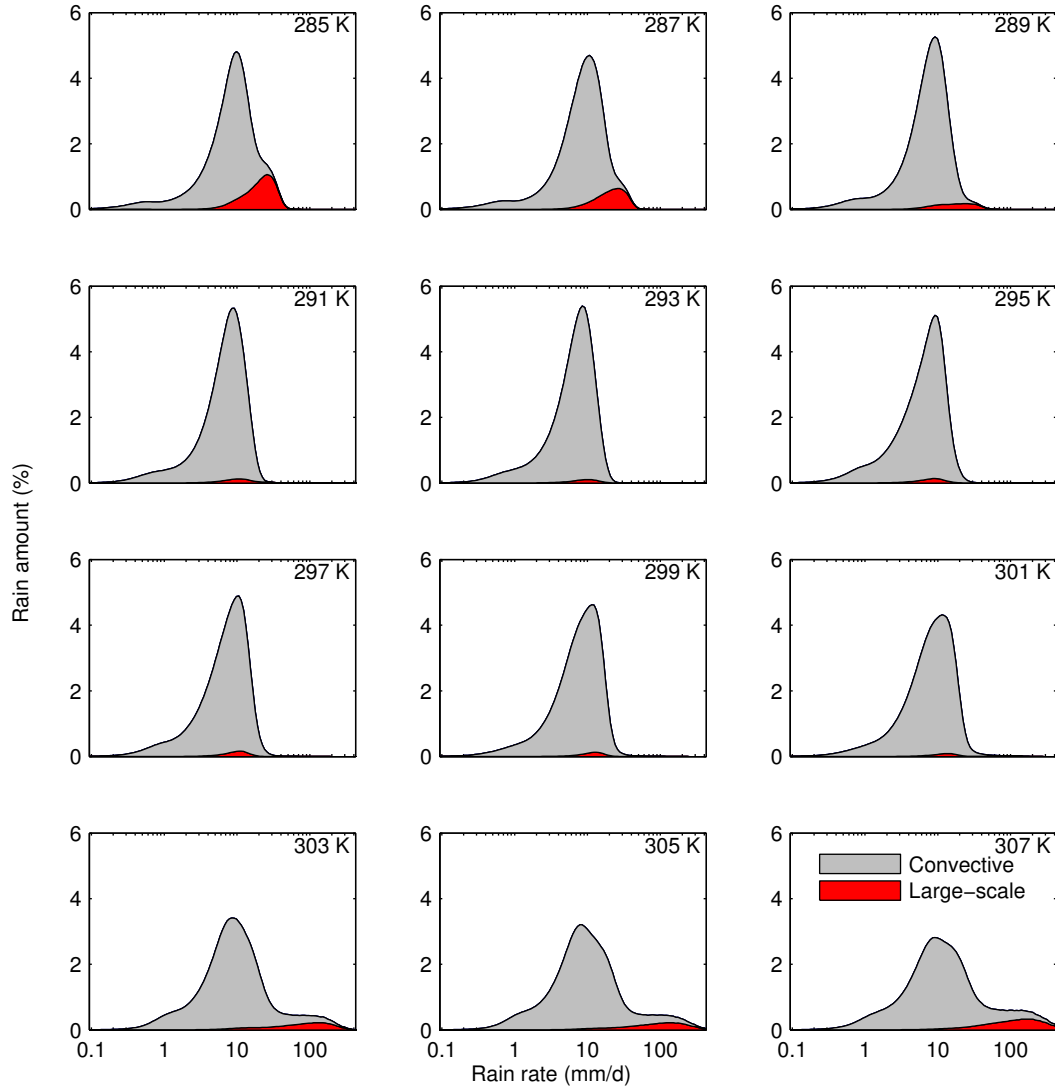


Figure S1. The rain amount distribution for each CAM5 global RCE simulation, the contribution from large-scale precipitation (red), and convective precipitation (gray).

Table S1. The change from one simulation to the next of mean precipitation and extreme precipitation (events over the 99th percentile threshold of daily precipitation, Fig. 2b,e).

SST (K)	Mean precipitation change (% K ⁻¹)	>99% precipitation change (% K ⁻¹)
287-285	3.0	-3.1
289-287	1.4	-11
291-289	-1.3	-7.8
293-291	2.1	-2.3
295-293	3.1	2.1
297-295	4.0	5.6
299-297	3.4	5.3
301-299	3.3	7.0
303-301	9.1	73
305-303	2.8	5.4
307-305	4.5	17

Table S2. Mean precipitation, moisture, extreme precipitation, components of the CAI, and fraction of total precipitation contributed by extremes for each simulation (Fig. 2a,c,d,f-i).

SST (K)	P (mm d ⁻¹)	q (g/kg)	q_{sat} (g/kg)	>99% P (mm d ⁻¹)	N (Events)	D (10 ⁶ m)	T (10 ⁹ events m d ⁻¹)	CAI (Events)	$f_{>99\%P}$ (%)
285	2.4	4.1	8.6	26	60	10	5.3	0.11	12
287	2.6	4.7	9.7	25	71	10.0	5.4	0.13	11
289	2.7	5.5	11	19	73	9.8	6.4	0.11	8.4
291	2.6	6.0	13	16	90	9.9	5.5	0.16	7.6
293	2.7	6.8	14	16	83	9.9	4.4	0.19	6.9
295	2.9	8.7	16	16	56	9.7	2.7	0.20	6.8
297	3.1	10.0	18	18	68	9.6	2.8	0.23	7.3
299	3.3	11	20	20	79	9.7	2.7	0.29	7.4
301	3.5	13	23	23	71	9.8	2.7	0.26	7.7
303	4.2	16	25	56	25	7.0	9.5	0.018	14
305	4.4	18	28	62	25	6.5	8.3	0.020	15
307	4.8	20	32	84	27	7.9	5.4	0.039	18

Table S3. Vertical velocity at 850 hPa and specific humidity from the lowest atmosphere level for each simulation (Fig. 3 a,b).

SST (K)	ω_{850} (Pa s ⁻¹)	q (g/kg)
285	-0.27	5.3
287	-0.22	5.9
289	-0.16	6.5
291	-0.14	7.0
293	-0.13	7.9
295	-0.12	9.8
297	-0.13	11
299	-0.13	13
301	-0.12	14
303	-0.24	17
305	-0.23	19
307	-0.28	22

Table S4. Extremes scaling and the effect of anomalous temperature profiles, vertical velocity, and temperature (Fig. 4).

SST (K)	Extremes Scaling (% K ⁻¹)	Anomalous temp. profile (% K ⁻¹)	Vertical velocity (% K ⁻¹)	Temperature (% K ⁻¹)
287-285	6.6	0.51	-7.6	6.6
289-287	6.3	0.50	-13	6.3
291-289	6.0	-1.2	-11	6.0
293-291	5.7	0.60	-10.0	5.7
295-293	5.4	4.1	-13	5.4
297-295	5.1	1.7	2.2	5.1
299-297	4.9	1.2	-2.0	4.9
301-299	4.6	1.5	-1.9	4.6
303-301	4.4	6.7	60	4.4
305-303	4.2	1.7	-0.067	4.2
307-305	4.0	3.2	8.6	4.0